Validity of the on-site spin-orbit coupling approximation

R. Cuadrado [1,2,*] R. Robles [1,†] A. García [3] M. Pruneda [1] P. Ordejón [1] J. Ferrer [4,5] and Jorge I. Cerdá [6,‡]

[1]*Catalan Institute of Nanoscience and Nanotechnology (ICN2), CSIC and BIST, Campus UAB, Bellaterra, 08193 Barcelona, Spain*
[2]*Universitat Autonoma de Barcelona, 08193 Bellaterra (Cerdanyola del Valles), Spain*
[3]*Institut de Ciència de Materials de Barcelona, ICMAB-CSIC, Campus UAB, 08193 Bellaterra, Spain*
[4]*Departamento de Física, Universidad de Oviedo, E-33007 Oviedo, Spain*
[5]*Centro de Investigación en Nanomateriales y Nanotecnología, Universidad de Oviedo-CSIC, 33940 El Entrego, Spain*
[6]*Instituto de Ciencia de Materiales de Madrid, ICMM-CSIC, Cantoblanco, 28049 Madrid, Spain*

Spin-orbit coupling (SOC) is generally understood as a highly localized interaction within each atom, whereby core electrons holding large J splittings transfer the SOC to the valence electrons of the same atom, while their direct impact on neighbor valence orbitals is usually small. Seivane and Ferrer [Phys. Rev. Lett. **99**, 183401 (2007)] proposed an approach within a tight-binding type *ab initio* framework assuming that the transfer of SOC from core to valence orbitals only takes place when both are on the same atom, leading to the so-called on-site approximation, which then has been successfully applied to a variety of systems. In this work we thoroughly test its general validity by confronting SOC related properties such as spin splittings, spin textures, or magnetic anisotropies calculated under the on-site approximation versus the more general approach where all the contributions to the SOC, including three-center integrals, are explicitly included. After considering a variety of systems with different dimensionalities, all presenting a strong SOC, we conclude that although the on-site approximation often provides accurate results, it breaks down in some systems where $5d$ electrons are close to the Fermi level due to their strong SOC and moderately large spatial extension. Furthermore, there are a few examples where subtle inaccuracies lead to qualitatively wrong conclusions, the most clear case being the doping of the topological surface state in $Bi_2Se_3(0001)$. Finally, magnetic anisotropy energies calculated under this approximation tend to be underestimated.

I. INTRODUCTION

The spin-orbit coupling (SOC) is a relativistic effect that arises from the interaction between the intrinsic magnetic moment of the electron and the magnetic field seen in its orbital motion around the nucleus [1,2]. The SOC is of paramount importance in numerous active research areas such as spin textures [3], topological insulators [4], spin Hall effects [5,6], magnetic anisotropy energies (MAEs) [7–11], Dzyaloshinskii-Moriya interactions [12–14], and spin-orbit transfer torques [15,16], among others. In fact, a new field known as spin orbitronics has emerged in the last years aiming to achieve efficient mechanisms for spin injection accumulation and manipulation [17] with potential use in ultralow power memories and computing and signal processing devices.

Along with the advent of this plethora of SOC-related phenomena, most codes based on density functional theory (DFT) had accomplished the implementation of spin-orbit interactions under different levels of approximation and accuracy. The main drawback in fully self-consistent calculations including SOC is the large increase of the computational cost caused by the spin mixing, whereby an $(N \times N)$ system transforms into a $(2N \times 2N)$ one, where N stands for the total number of basis orbitals. Therefore, accurate all-electron DFT calculations using a fully-relativistic (FR) Hamiltonian in the Schrödinger equation are currently restricted to small systems involving at most a few tens of atoms [18]. The replacement of core electrons by pseudopotentials (PPs) [19,20] has become a standard approximation [21–24] in order to significantly reduce N, making calculations for large systems more tractable. Although traditionally most PP-based formalisms exploited only the scalar-relativistic (SR) part of the PPs generated from all-electron FR atomic calculations, Hemstreet *et al.* showed almost thirty years ago how the SOC part could be incorporated into the electronic Hamiltonian in an efficient way [25]; in previous works we have referred to it as the fully relativistic pseudopotential formalism (FR-PP) [26]. In essence, within the FR-PP, the angular part of the PP of a given atom k, V_k^{ps}, is expressed in the $|j = l \pm \frac{1}{2}, m_j\rangle$ basis and the SOC felt by the valence states solely arises from their interaction with the SO part of these PPs which induces spin mixing via nonvanishing $\langle \mu, \sigma | V_k^{so} | \nu, \sigma' \rangle$ matrix elements, where μ and ν index the elements of the basis set (plane waves, atomic orbitals, wavelets,...) and $\sigma = \uparrow, \downarrow$. In the context of calculations using atomic orbitals as basis sets, where the orbitals are centered on the atoms and are the product of a radial function times a

spherical harmonic that describes the angular part (so-called linear combination of atomic orbitals or LCAO approaches), the orbitals μ and ν may belong to different atoms than k, the only requirement being that their overlaps with V_k^{so} are not null. In order to avoid the calculation of these three-center integrals, the PPs are typically expressed in their fully non-local form [27]. The FR-PP formalism has been successfully implemented and is currently actively used under both plane wave [24] and LCAO [3,21,28,29] DFT codes.

Within the LCAO framework, a further simplification named as the on-site approximation was introduced by Seivane and Ferrer [30] whereby only the $\langle \mu | V_k^{so} | \nu \rangle$ matrix elements with $|\mu\rangle$ and $|\nu\rangle$ belonging to the same atom k as V_k^{so} are considered, while the rest of the interatomic hopping terms are discarded. The justification relies on the short-ranged character of the radial part of the spin-orbit pseudopotential. The approximation leads to a one-center radial integral while the angular integrals can be analytically solved for the nonvanishing elements. The on-site approximation has been applied to a number of systems, ranging from the SOC induced valence band splittings of semiconductors to the MAEs of metallic nanoparticles [30,31].

However, no thorough study of the accuracy of the on-site approximation has yet been performed. Although deviations from the full FR-PP approach are expected to be small, hopping terms can add up to produce effects comparable to those of the on-site terms [32], and therefore it is important to assess the range of validity of the on-site approximation. The implications are also relevant when considering tight binding (TB) models including SOC [33,34]. For instance, under the on-site approximation, one would expect that the SOC only affects on-site energies with corrections of the form $\epsilon_{l,m,m'}^{SO,\sigma\sigma'}$, whereas the off-site contributions would additionally lead to SOC dependent transfer integrals, $t_{lm,l'm'}^{SO,\sigma\sigma'}$.

In this work we present a detailed analysis of the accuracy of the on-site approximation considering several systems with different dimensionalities (from 0D to 3D), all of them presenting a strong SOC. We address SOC related properties such as MAEs, Rashba splittings, spin textures, and (topological) surface states. All calculations have been performed with the SIESTA [21] LCAO code, which in its recent versions [35] features both the full FR-PP and the on-site approximation. We employ the same calculation parameters for each system in order to ensure that any differences can be solely ascribed to the neglect of off-site terms in the on-site approximation.

The paper is structured as follows. In Sec. II we describe briefly the theoretical formula behind the FR-PP formalism and the on-site approximation, as well as some general remarks concerning the actual implementation in SIESTA. In Secs. III and IV we present the different SOC systems considered, showing the excellent accuracy of the on-site approximation in most of the cases but also emphasizing the few failures that we have found. Finally, Sec. V summarizes the main conclusions of this work.

II. THEORY

Within a PP-DFT formalism, the Kohn-Sham Hamiltonian may be expressed as:

$$\hat{H}^{KS} = \hat{T} + \hat{V}^{ps} + \hat{V}^H + \hat{V}^{XC} \qquad (1)$$

with being $\hat{T}$ the kinetic energy operator, $\hat{V}^{ps}$ the PP contribution, and $\hat{V}^H$ and $\hat{V}^{XC}$ the Hartree and exchange-correlation potentials, respectively. $\hat{V}^{XC}$ and the SO part of $\hat{V}^{ps}$ ($\hat{V}^{SO}$) are the only spin-dependent operators that couple both spin components.

Kleinman [20] showed how the norm-conserving PP formalism could be extended to include all relativistic corrections up to order α^2, where α is the fine structure constant, by constructing J-dependent PPs from the all-electron solutions of the major component of the Dirac equation for isolated atoms:

$$\hat{V}^{ps} = \sum_{lJ} V_{lJ}^{ps}(r) \sum_{m_J=-J}^{+J} |lJm_J\rangle\langle lJm_J| \qquad (2)$$

with $J = l \pm 1/2$.

If an LCAO basis set is employed, $\{|\mu\rangle\}$, then the matrix elements of the $\hat{V}^{ps}$ operator take the form:

$$V_{\mu\nu}^{ps} = \sum_k \langle \mu | \hat{V}_k^{ps} | \nu \rangle \qquad (3)$$

where we have introduced the subindex k indicating the atom to which each $\hat{V}^{ps}$ belongs. The main problem with expression (2) is that it has a semilocal character, in the sense that it is local in the radial part and nonlocal in the angular part [25] and, hence, it requires the computationally expensive evaluation of three-center integrals since the AOs $|\mu\rangle$ and $|\nu\rangle$ need not be located at the k site. After taking the following J-weighted sum and difference:

$$V_l^{SR}(r) = \frac{1}{2l+1}[(l+1)V_{lJ+}(r) + V_{lJ-}(r)] \qquad (4)$$

$$V_l^{SO}(r) = \frac{2}{2l+1}[V_{lJ+}(r) - V_{lJ-}(r)] \qquad (5)$$

(where $J_\pm = l \pm 1/2$), equation (2) may be rewritten in terms of a scalar-relativistic (SR) and a spin-orbit contribution as:

$$\hat{V}^{ps} = \hat{V}^{SR} + \hat{V}^{SO}$$
$$= \sum_{lm} |l,m\rangle[V_l^{SR}(r) + V_l^{SO}(r)\mathbf{L}\cdot\mathbf{S}]\langle l,m|. \qquad (6)$$

It is common practice in scalar-relativistic DFT calculations to transform the SR part into a local plus a sum of fully nonlocal operators following Kleinman-Bylander [27]:

$$\hat{V}^{SR} = V^{local}(r) + \sum_{lm} |v_l;lm\rangle\langle v_l;lm| \qquad (7)$$

so that only two-center integrals, $\langle \mu | v_l; lm \rangle$, are now involved.

A. The fully relativistic pseudopotential formalism

Hemstreet *et al.* [25] deduced fully nonlocal forms for the SR and SO pseudopotential operators. Inspired by their work, alternative albeit equivalent expressions were deduced by Cuadrado *et al.* [26]; here, the full $\hat{V}^{ps}$ operator is transformed into a Kleinman-Bylander form in the $\{|lJm_j\rangle\}$ basis:

$$V^{ps} = V^{local}(r) + \sum_{lJm_J} |v_{lJ};lJm_J\rangle\langle v_{lJ};lJm_J| \qquad (8)$$

thus only requiring two-center integrals between projectors and basis orbitals, $\langle \mu | v_{lJ}; lJm_J \rangle$. Although the matrix elements of V^{ps} are sufficient to solve the problem, and the decomposition in SR and SO terms is not necessary, these terms can nevertheless be obtained if needed for further analysis. By computing at the same time the $\hat{V}_{\mu\nu}^{SR}$ matrix elements via Eq. (7) with the same choice of $V^{local}(r)$ as in (8), it is straightforward to extract the SO contribution from the difference: $V_{\mu\nu}^{SO} = V_{\mu\nu}^{ps} - V_{\mu\nu}^{SR}$. This FR-PP method takes into account all interactions $\langle \mu | \hat{V}_k^{ps} | \nu \rangle$ between the PP at site k and all neighboring AOs and provides a rigorous account of SOC within the context of the underlying pseudopotential and LCAO approximations.

B. The on-site approximation

In the on-site approximation developed by Seivane and Ferrer [30], the standard expression (7) for the SR part is retained, while $\hat{V}^{SO}$ is approximated as a fully local operator by only considering intra-atomic matrix elements, that is, $\langle \mu | \hat{V}_k^{ps} | \nu \rangle$ terms where both $|\mu\rangle$ and $|\nu\rangle$ belong to atom k, and neglecting all others. The justification lies in the fact that the $V_l^{SO}(r)$ potentials are short ranged.

C. General remarks about the implementation of SOC in siesta

Both the full FR-PP formalism and the on-site approximation have been implemented in SIESTA [35] as separate modules. Nevertheless, we have tested both implementations by removing in the full FR-PP routine any SOC interactions involving orbitals not belonging to the same site as the PP, yielding results indistinguishable from those obtained with the on-site specific routine.

We also note that SIESTA, as well as most common LCAO codes, employs the spherical harmonics $Y_{lm}(\hat{\mathbf{r}})$ in their real form, obtained as a linear combination of complex spherical harmonics. Therefore, the Clebsch-Gordan coefficients involved in the angular $\langle lm | lJm_J \rangle$ integrals require a further unitary transformation [26,30].

Once the Hamiltonian including the SOC part has been solved self-consistently, the spin-orbit contribution to the energy is given by:

$$E^{SO} = \text{Tr}[\hat{\rho}\hat{V}^{SO}] = \sum_{\mu\nu} \sum_{\sigma\sigma'} \rho_{\mu\nu}^{\sigma\sigma'} V_{\nu\mu}^{SO,\sigma'\sigma}. \quad (9)$$

Although the imaginary parts of the diagonal spin boxes of the density matrix, $\text{Im}\{\rho_{\mu\nu}^{\sigma\sigma'}\}$, do not contribute to the magnetic moment $\mathbf{m}(\mathbf{r})$, they cannot be neglected since they do contribute to the SOC energy, E^{SO}, and therefore to the total energy.

Due to the small contribution of E^{SO} to the total energy, the level of precision required to perform an accurate fully relativistic self-consistent calculation is quite demanding. This is specially true for the calculation of MAEs, where energy differences between two spin-quantization axis are typically in the meV (and sub-meV) range. In such calculations, the tolerance in the self-consistent criteria (either related to the Hamiltonian, density matrix, or both), the k-point sampling or the size of the real space grid (Mesh Cutoff) must be carefully converged for each specific system to ensure accurate results.

In addition, and as shown in Ref. [26], inclusion of nonlinear core corrections [36] in the PPs with rather small matching radius is in general quite relevant to achieve accurate MAE values. This, in turn, requires finer real space grids. Last, we mention that in SIESTA it is possible to either construct the fully relativistic Kleinman-Bylander projectors from PPs in semilocal form or directly read them from appropriately generated PSML files, as provided by the Pseudo-Dojo project [37,38].

D. Details of the calculation parameters

In all SIESTA calculations to be shown in the next sections we employed the GGA [39] for the XC functional and fully relativistic PPs including nonlinear core corrections. Specifically, we used core radii of 1.15 Å, 1.52 Å, 2.01 Å for Bi ($6s^2 6p^3 6d^0$), 1.19 Å, 1.44 Å, 0.66 Å for Au ($6s^1 6p^0 5d^{10}$) and Pt ($6s^1 6p^0 5d^9$), 1.49 Å, 1.52 Å, 1.25 Å for W ($6s^2 6p^0 5d^4$), 0.84 Å, 1.05 Å, 1.57 Å for Te ($5s^2 5p^4 5d^0$), and 1.06 Å, 1.31 Å, 0.31 Å for Fe ($4s^2 4p^0 3d^6$), respectively. For the basis set of the atoms' valence electrons we used strictly localized numerical AOs generated according to the double-ζ polarized (DZP) scheme with confinement energies ranging between 100–200 meV [40]. The electronic temperature—kT in the Fermi-Dirac distribution—was set to small values between 1–25 meV. Real-space integrals were computed over three-dimensional grids with a resolution of 1500–2000 Ry. The Brillouin zone sampling typically involved between 100–2500 k points.

The convergence tolerance in the self-consistent loop for the density matrix was set to 10^{-6} or to 1 meV if the Hamiltonians were mixed instead. The geometric optimizations were performed using the conjugate gradient method until forces on atoms were less than 0.02 eV/Å. The optimizations have been performed at the SR level—that is, without SOC.

Selected results have been compared with calculations done with the VASP code, which is commonly used for SOC calculations [41]. We have used the same XC functional [39] and geometries as in SIESTA. Plane-wave energy cutoffs were taken between 250–400 eV, with additional tests up to 1000 eV.

Furthermore, in order to achieve a precise description of the surface states in several systems, we considered true semi-infinite surfaces via Green's function matching technique as implemented in the GREEN code [42,43] and its interface to SIESTA. In these cases, instead of the usual band structure, we calculated **k**-resolved surface projected density of states maps, PDOS(**k**,E), which allows us to resolve the bulk gap regions unambiguously. High resolution maps were computed employing energy and k grids of 2 meV and 0.003 Å^{-1}, respectively, while the imaginary part entering the Green's function, which determines the broadening of the surface states, was set to 2 meV.

III. ELECTRONIC BAND STRUCTURES

A. Isolated helical Te chain

The first case we consider is a helical isolated chain of tellurium atoms which was recently studied by Han *et al.* [44]. This one-dimensional system was shown to be
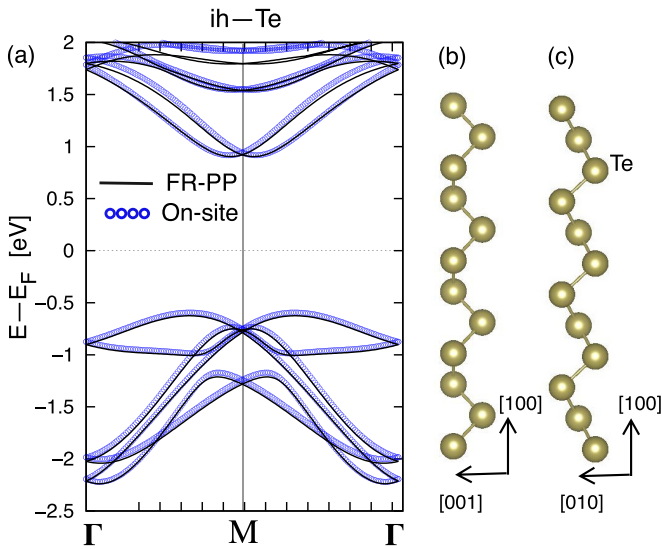
FIG. 1. (a) Electronic band structure of isolated hexagonal Te chain. Black solid curves represent the bands obtained by means of the full FR-PP method and blue ones using the on-site approximation. (b),(c) Schematic side views of the chain from two different directions.

FIG. 2. (a)–(c) PDOS($\mathbf{k}$,E) maps projected on the layers close to the edge of a semi-infinite Bi(111) bilayer calculated over the entire Brillouin zone without including SOC (a), and including SOC with the full FR-PP formalism (b), and using the on-site approximation (c). The inset shows top and side views of the system with the arrows indicating the semi-infinite direction. The spin texture, in the form of $S_{y/z}(k, E)$ maps, is shown in (d) and (f) for the full FR-PP calculation and in (e) and (g) for the on-site approximation. In (d)–(g) white/black tones indicate positive/negative $S_{y/z}$ values, while the gray background corresponds to $S_{y/z} = 0$ areas.

dynamically stable and to present a giant Rashba splitting [44]. Figure 1 displays the 1D band structure for our optimized geometry which coincides with that of Ref. [44]. In the figure we simultaneously present the bands calculated with the full FR-PP method and the on-site approximation. The agreement between the two (as well as with those reported in Ref. [44]) is excellent, with deviations of just a few tens of meV. Larger differences are only found for an empty band just below +2 eV. Notice in particular how the giant Rashba splitting of the highest occupied band is perfectly reproduced, both in terms of the spin splitting in energy as well as the k shift.

B. Zigzag surface at a Bi bilayer

Our next system is a semi-infinite 2D material consisting of a truncated Bi(111) bilayer exposing a zigzag edge. The structure is constructed by first building a 22-atoms thick ribbon with the atoms initially at the positions of the ideal infinite 2D bilayer ($a = 4.60$ Å). We then optimize the positions of the six atoms closest to the edge of the ribbon, leaving the rest fixed. The most prominent feature in the relaxed structure is a large ∼0.6 Å inward shift of the atoms at the edge towards the inner ones in order to strengthen their bonds, which is also accompanied by an increase in the buckling between them from 1.68 Å to 2.0 Å. Next, and as shown in Fig. 2, we have modeled the bilayer edge with a semi-infinite geometry after matching via Green's function techniques the ribbon containing the relaxed edge to an semi-infinite bulklike bilayer (see Sec. II D for further details).

In Fig. 2(a) we present the electronic structure around the Fermi level projected on the surface atoms for a calculation without SOC. A spin degenerate edge state runs across the band gap of the entire BZ crossing the Fermi level four times, in good accordance with the similar calculation of Ref. [45]. In panel (b) we present the analogous calculation including
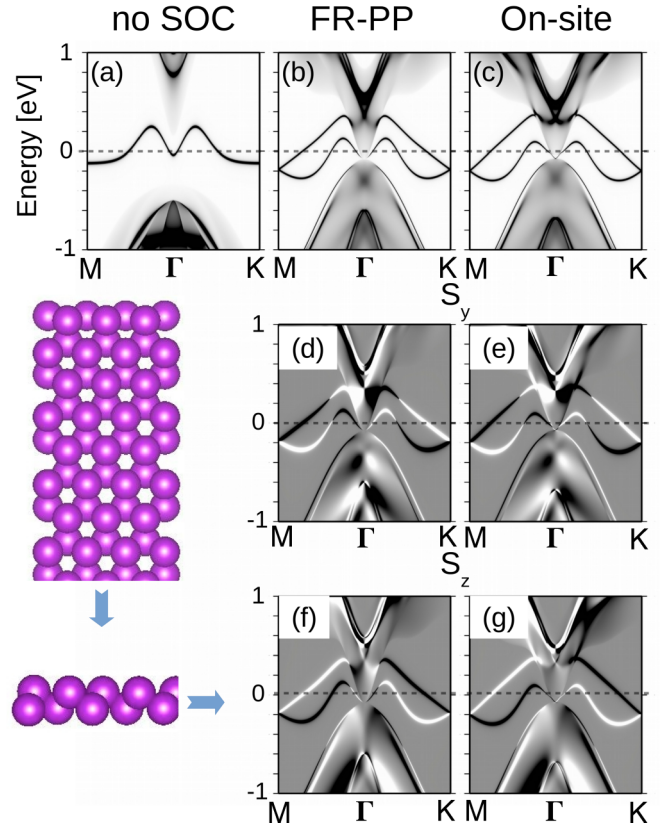
SOC at the full FR-PP level. The topologically trivial edge state now appears spin split while the gap is removed. Indeed, at the equilibrium lattice constant, the bulk 2D Bi(111) bilayer is at the turning point towards a topological state as it becomes metallic as the gap closes when SOC is included (not shown). This is at contrast with the 1D nanoribbon case; for instance, Li *et al.* [45] found a sizable gap for a 73 Å wide zigzag nanoribbon which we ascribe to the interaction between the two edges, still present even for such a wide nanoribbon. Upon comparison with the on-site calculation, shown in panel (c), we again find perfect agreement with only very subtle differences; for instance, the upper edge state inside the conduction band cone (resonance) is clearly more intense.

Surface projected spin textures are presented in panels (d),(f) and (e),(g) for the full FR-PP and on-site cases, respectively; the S_x component is omitted since, due to mirror symmetry, it vanishes. Remarkably, we find that the on-site approximation accurately reproduces this rich spin texture, presenting inversions of the S_y component at the correct k locations for the edge states.
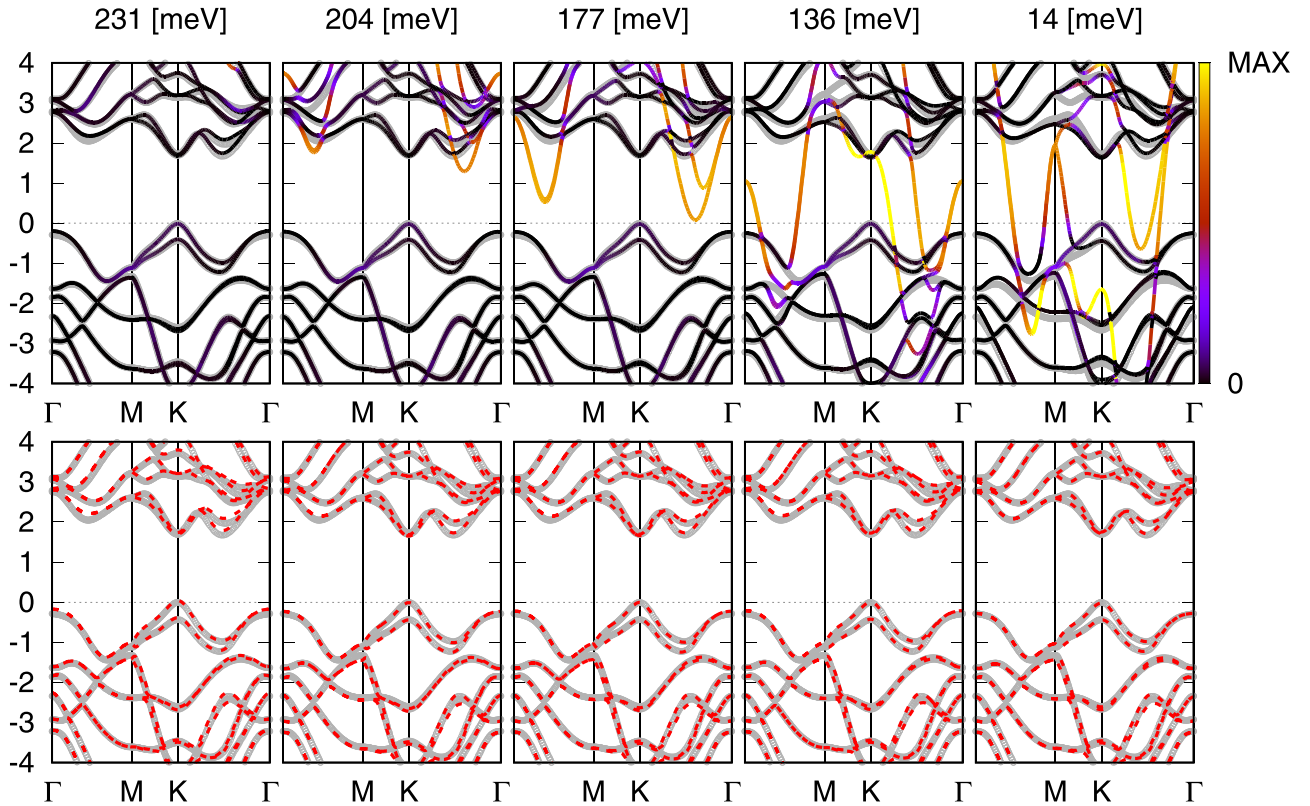
FIG. 3. Electronic band structure for a WS_2 monolayer within on-site approximation (top, solid color-coded lines) and FR-PP formalism (bottom, red dashed lines). Different panels correspond to different basis' range, obtained from localization energies determined by SIESTA's PAO.EnergyShift (in meV). The smaller the EnergyShift, the longer the cutoff radii for the atomic orbitals. A better basis is usually obtained with longer orbitals. The color code at the top right is used to represent the weighted projections on W $6p$ orbitals for the on-site approximation and reveals the character of the band that induces the metalization of the system (black corresponds to small contribution on W $6p$ and yellow to maximum contribution). The gray thick lines in the background for top and bottom panels show the results for an optimized (fixed) basis set [47] under the on-site description.

C. WS_2 monolayer: Range of the basis orbitals

We illustrate the influence of the localization of the basis set on the performance of FR-PP and on-site approximation by calculating the band structure of a monolayer of a transition metal dichalcogenide, WS_2 (Fig. 3). As for surfaces, it is known that the extension of the electronic wave functions in monolayers towards the vacuum requires longer atomic orbitals to give accurate results [46]. Longer orbitals means larger interactions with neighbor orbitals and larger off-site terms in the SO operator. We use two alternative bases: One set is automatically generated by SIESTA using different values of the confinement energy (PAO.EnergyShift between 230 and 14 meV, which results in maximum cutoff radii between 3.52 and 4.76Å, respectively); the second basis was carefully tuned for the on-site approximation by Roldán *et al.* [47]. While for relatively short basis both the on-site (top panels) and the FR-PP formalism (red dashed lines in lower panels) give essentially indistinguishable band structures, substantial differences are evident for the longer orbital basis. In particular, a band with p-type character crosses from high energies down below the Fermi level as the orbital cutoff radii increases, erroneously driving the system metallic with the on-site

description. Mulliken population analysis shows that there is non-negligible overlap between W neighboring atoms. As the basis radial function increases, this approximation forces an internal redistribution of charges between $6s$ and $6p$ orbitals, which also involves $3s$ and $3p$ orbitals of near S atoms. Note that this does not affect the S_{3p}-W_{5d} hybridization that is responsible for the SO splitting of the valence band at K. This illustrates that for the on-site approximation to be valid, the range of localization of the support orbitals must comply with the conditions of negligible, or small, off-site contributions.

D. Bi_2Se_3(0001) surface

In this subsection we consider the Bi_2Se_3 dichalcogenide as it stands as a paradigmatic topological 3D insulator, given its large gap. In order to retrieve the topological surface states (TSS) we have employed a (0001) oriented slab containing up to six quintuple layers (QLs), since for this thickness the interaction between the TSSs at each side of the slab is known to be negligible [28]. We do not model the surface as a semi-infinite system since we will compare the SIESTA-derived electronic structure with that obtained with the VASP plane-wave code
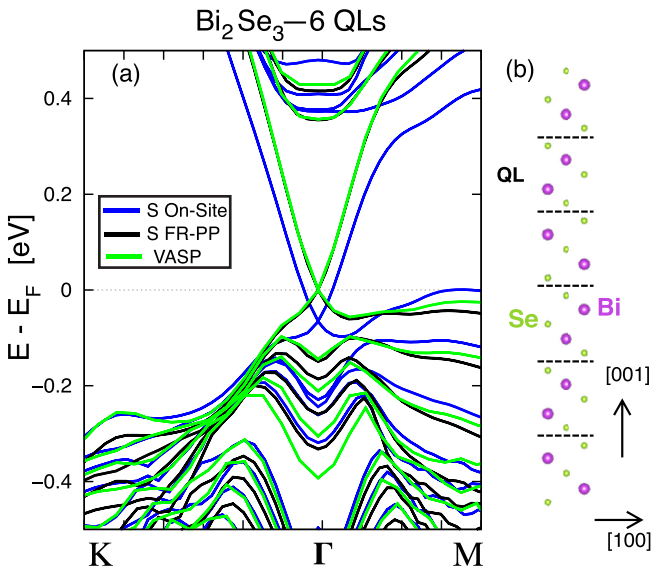
FIG. 4. (a) Electronic bands structure for 6 QLs Bi_2Se_3 slab. Three different curves are depicted and represent the SIESTA results with the on-site approximation (blue) and the full FR-PP calculation (black) and VASP calculations (green). (b) Schematic side view of the 6 QLs Bi_2Se_3 slab unit cell. Pink spheres represent Bi atoms whilst green ones the Se species. For clarification, dashed black lines separate each QL.

[22] for the same slab geometry. The comparison between the band structures calculated with VASP (green lines) and SIESTA using the full FR-PP formulation (black) and the on-site approximation (blue) is displayed in Fig. 4(a). If we focus on the TSSs crossing the band gap between −0.1 and 0.35 eV, one immediately observes a very good match between VASP and our FR-PP results, with the Dirac point where the upper and lower cones meet located precisely at the Fermi level due to charge neutrality requirements. The on-site approximation also reproduces the TSSs but with the Dirac point located clearly below the valence band maximum (at around −80 meV) and, hence, not pinned any more at the Fermi level. Although in general a deviation of several tens of meV does not seem too relevant—for instance, similar differences can be seen in the valence band at Γ between the plane-wave and FR-PP cases—in this particular case it has fundamental consequences as the on-site approximation would erroneously predict an *n*-type doped TSS.

E. (111) surfaces of 5*d* metals

In this subsection we examine the capability of the on-site approximation to correctly describe the surface states (SSs) hosted by several (111) surfaces of heavy 5*d* *fcc* metals, namely: Au, Ir, and Pt. For all of them we have again modeled the surfaces as semi-infinite systems first determining the relaxed surface interlayer spacings via geometry optimizations of 10–11 layers thick (1 × 1) slabs.

Figure 5 shows the *k*-resolved DOS projected on the first layers of the Au(111) surface around the Γ point, with panels (a) and (b) corresponding to the full FR-PP formalism and the on-site approximation, respectively. The well known Shockley *sp* surface state [48] is clearly visible in both maps as
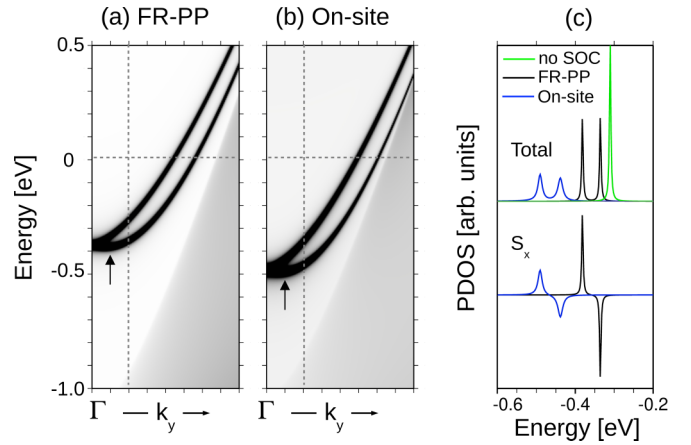

FIG. 5. PDOS(**k**,E) map projected on the first three layers of a semi-infinite Au(111) surface calculated under the (a) full FR-PP formulation and (b) the on-site approximation. (c) Top: EDC plots extracted at the *k* point $k_y = 0.03$ Å^{-1} which corresponds to the minimum of the parabolic band and is highlighted with an arrow in (a) and (b). Also shown by the green line the EDC for a calculation without SOC. Bottom: *y* component of the spin polarization density, S_y, for the full FR-PP formulation and the on-site approximation.

two Rashba split parabolas crossing the gap region. At first sight, the main difference is the onset of the SS, which appears 0.1 eV towards larger binding energies in the on-site case. Otherwise, the splitting and dispersion of the SSs are very similar between the two formalisms. However, a closer look into the spectra via energy dispersion curves (EDCs) brings in further discrepancies. In the top panel of Fig. 5(c) we present EDCs extracted for the *k* point marked by an arrow in panels (a) and (b), as well as that obtained for a calculation without SOC (green line). The effect of the SOC is to shift the SS to lower energies and induce a spin splitting which for this *k* point is around 50 meV (for reference, the splitting at the dashed vertical line in the figure is around 100 meV, which is in agreement with previous theoretical and experimental estimations [49,50]). Under the on-site approximation the shift is ∼109 meV larger, while the splitting is only marginally larger. On the other hand and as expected from symmetry arguments, the helical (Rashba) character of the SS spin texture is not disrupted by the on-site approximation. This is seen at the bottom of Fig. 5(c), where the in-plane tangential component of the spin (S_x) takes opposite values at each branch while the radial in-plane component vanishes and the out-of-plane is negligible (the latter two not shown). Figure 6 shows analogous surface PDOS(**k**,E) maps as in Figs. 5(a) and 5(b) but for the Pt(111) and Ir(111) surfaces—panels (a),(b) and (c),(d), respectively. At contrast with the noble metal Au case, here the 5*d* bands cross the Fermi level while, apart from a 0.6 eV shift, their full FR-PP band structures show very similar features among them. In particular, both present a ∼1.4 eV gap in a narrow *k* region around the high-symmetry K point which hosts two pairs of spin-split SSs indicated by the blue arrows in panels (a) and (c); one is very close to the top edge of the gap (located at −0.7 eV in Pt and −0.15 eV in Ir) and has a very small spin splitting, and the other is near the bottom (around −1.7 in Pt and −1.4 eV in Ir showing a
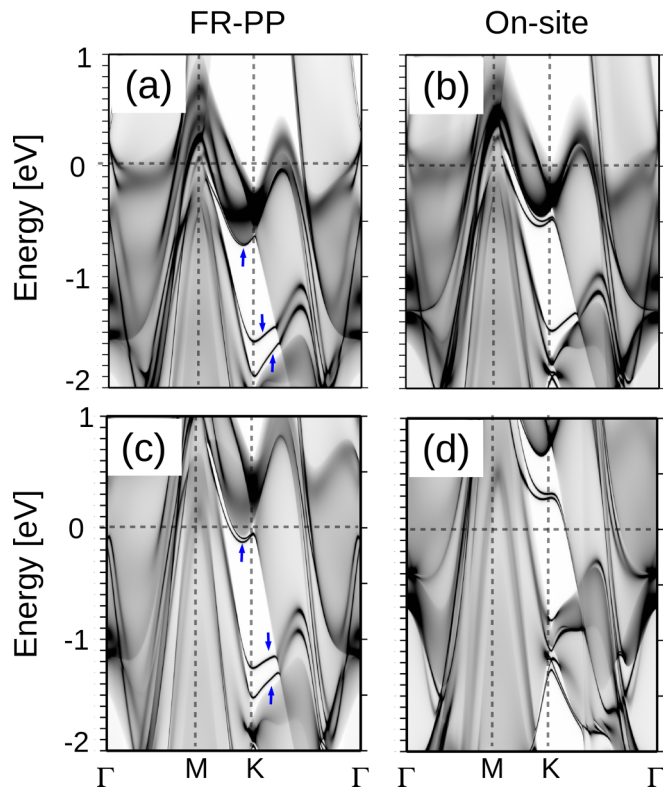
FIG. 6. (a),(b) PDOS($\mathbf{k}$,E) maps projected on the surface planes of a Pt(111) semi-infinite surface calculated under the full FR-PP formulation and the on-site approximation, respectively. (c),(d) Same as (a),(b) but for the Ir(111) surface. Small blue arrows in (a) and (c) indicate surface states crossing the K point.

large 0.2–0.3 eV spin splitting. The corresponding electronic structures obtained under the on-site approximation, shown in the right panels (b) and (d), also reproduce this gap, but clearly shifted towards higher energies with respect to the FR-PP counterparts. In the case of Ir(111) this shift is as large as 0.6 eV, so that the upper SS lies above the Fermi level (becomes empty) while the lower one falls into the continuum of bulk bands (becomes a resonance), thus yielding a highly inaccurate picture of the electronic structure. For Pt(111) the shift is reduced to 0.25 eV but we still regard the quality of the on-site bands as rather poor.

F. Bulk GeTe

We end this section considering a bulk 3D system with a broken space inversion symmetry, so that spin degeneracy can be removed due to the SOC interaction [51]. We have chosen as a model system the monochalcogenide GeTe insulator as it is known to exhibit a large Rashba effect [52]. GeTe stabilizes in a ferroelectric rhombohedrally distorted rocksalt structure with space group $R3m$. Figure 7 shows the energy dispersion of the valence and conduction bands around the Fermi level. This time the on-site bands (blue lines) yield an almost perfect agreement with the full FR-PP case (dark), accurately reproducing the strong Rashba splitting for both bands at the Z point, while small deviations appear only in the valence band as one moves towards the A point.
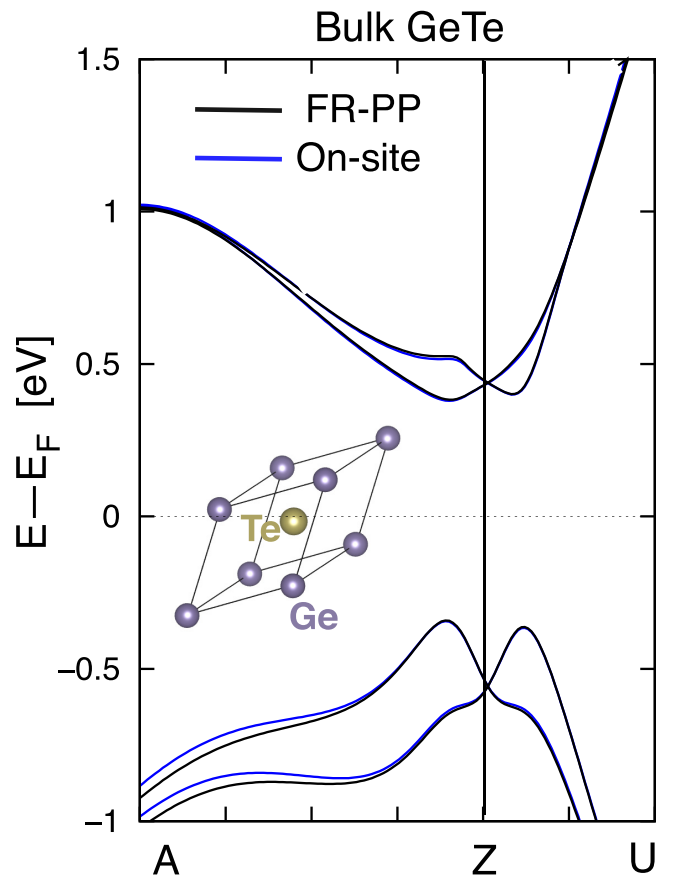

FIG. 7. Electronic bands structure of bulk GeTe. Similarly to the plots of previous figures, blue and black solid lines represent the SIESTA results with the on-site approximation and the full FR-PP calculation, respectively. The inset shows the schematic crystal structure of distorted GeTe with the polar axis along the [111] direction.

IV. MAGNETIC ANISOTROPY ENERGIES

MAE is defined as the difference in total energy between the easy and hard magnetization axes of a system. In this section we address the capability of the on-site approximation to obtain MAEs close to those derived from the full FR-PP approach. We note that reproducing energy differences at the meV (or even sub-meV) level is, in general, a more stringent test than the comparison between band structures.

A. Pt dimer

We first analyze the MAE for the Pt dimer. We have optimized the bond distance obtaining a value of 2.27 Å. The dimer was located along the X axis and two SC calculation along X and Z spin quantization axis were performed for the on-site approximation and the full FR-PP formulation. The energy differences, $E_x - E_z$, were of 206 meV and 200 meV, respectively. Both calculations give similar values of the MAEs and predict the easy axis along the bond axis as previously reported by Seivane and Ferrer [30].

B. FePt-L1$_0$ bulk alloy

The binary FePt-L1$_0$ alloy is formed by alternating planes of Fe and Pt with square lattice geometry (see Fig. 8, left),
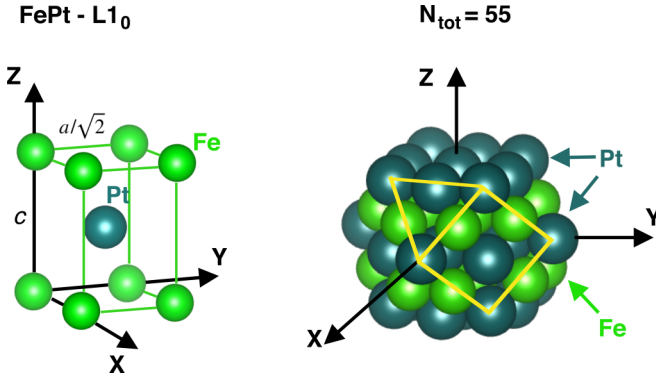
FePt - L1$_0$

N$_{tot}$ = 55

FIG. 8. (Left) Schematic picture of the FePt-L1$_0$ bulk unit cell and its characteristic lattice values: *a* and *c*. Notice that the in-plane diagonal of the unit cell corresponds to the lattice constant while the edge is a/$\sqrt{2}$. (Right) L1$_0$ cuboctahedral 55 NP structure. Superimposed yellow solid lines show two kinds of surfaces (square and triangle). Cartesian frame *X*, *Y*, and *Z* is represented by three black lines.

leading to a structure with slightly different in-plane *a* and out-of-plane *c* lattice constants. As a result of the lattice parameters optimization we obtained $a = 3.92$ Å and $c/a = 0.96$.

The upper part of Table I shows the energy difference between the solutions with magnetization along the *X* and *Z* directions, $\Delta E_{x-z} = E_x - E_z$ using SIESTA, VASP, a full-potential (FP) version of the linear-muffin-tin orbital (LMTO) method [53], and the work of Khan *et al.* [54] in which they obtained the MAE by means of SPRKKR and WIEN2K (PBE-GGA). The on-site approximation underestimates the MAEs by 15% with respect to the full FR-PP values, which coincide with those obtained with FP-LMTO and are just 5% smaller than those obtained with VASP. Part of the discrepancies between our results and the ones obtained by Khan *et al.* [54] could be due to slightly different lattice constants used in the calculations.

We have also calculated the MMs and orbital magnetic moments (OMs) of Fe and Pt atoms in the alloy. Both SOC implementations give similar values of MM$_{Fe}$ = 3.2 μ_B and MM$_{Pt}$ = 0.2 μ_B. In agreement, VASP provides 3.03 μ_B and 0.31 μ_B for Fe and Pt, respectively. The OMs are depicted in Table I.

C. FePt-L1$_0$ cuboctahedral nanoparticle

Next, we have considered a nonperiodic system consisting of a cuboctahedral FePt nanoparticle (NP) composed of 55 atoms following a L1$_0$ stacking. This kind of NP belongs to the so-called magic cluster sizes where the total number of atoms follows the relation $N_{tot} = (10n^3 + 15n^2 + 11n + 3)/3$, where *n* represents the number of geometrical closed shells which, in our case, is $n = 2$ (see right panel in Fig. 8). The total number of atoms for each species is then given by $N_M = (5n^3 + 6n^2 + 4n)/3$ for the magnetic (M), and $N_{NM} = (5n^3 + 9n^2 + 7n + 3)/3$ for the nonmagnetic (NM) species, i.e., $N_M = 24$ and $N_{NM} = 31$. The initial structure of the NP was built using the FePt-L1$_0$ bulk experimental values [53] (3.86 Å and 0.98, respectively), and the geometry was subsequently fully relaxed. The square box where the NP was simulated had 25 Å of side avoiding the neighboring interaction with replicas in adjacent cells.

Due to the cuboctahedral shape of the NP we have calculated the total energy along three different spin quantization axes defined by the spherical angles (θ, ϕ), namely: $(0°, 0°)$, $(90°, 0°)$, and $(90°, 45°)$. In the following, we will label these directions as *z*, *x*, and *xy*, respectively, and the energy difference as: $\Delta E_{x-z} = E_x - E_z$ and $\Delta E_{xy-z} = E_{xy} - E_z$. The calculated values are shown in Table I for the on-site approximation and the full FR-PP, as well as for VASP. All predict correctly the easy axis of the NP that lies out-of-plane $(0°, 0°)$. Comparing the largest energy difference we observe that, while the full FR-PP MAE is $\Delta E_{xy-z} = 37.2$ meV, on-site predicts a smaller value by around 30% (25.8 meV) and VASP a 25% larger value (50.0 meV). As in the case of the bulk material, we conclude that the on-site approach underestimates the MAE values of this kind of cuboctahedral NP.

We have also obtained the magnetic moments (MMs) of each of the Fe and Pt atoms of the NP for the case in which the magnetization is along *z*. We summarize their behavior taking into account whether the atoms are in the core or at the surface. Whereas the MMs of the core atoms of both Fe and Pt species present similar values and alignment, Fe atoms at the surface present small tilts along *x* or *y* directions within the range of 0.1–0.4 μ_B in the full FP-PP calculation and between 0.04 and 0.27 μ_B for the on-site approximation. The induced MMs of surface Pt atoms present similar dispersion for both formalisms between 0.2 and 0.4 μ_B along the Z direc-

TABLE I. Energy difference (in meV) and orbital magnetic moments (in μ_B) between different magnetization orientations for the FePt-L1$_0$ bulk alloy and the Fe$_{24}$Pt$_{31}$ NP obtained using the on-site approximation and the FR-PP formulation as implemented in SIESTA, compared to VASP, FP-LMTO, SPRKKR, and WIEN2K(PBE-GGA).

System	Method	ΔE_{x-z}	ΔE_{xy-z}	$\mu_{orb}^{(M||z)}$(Fe)	$\mu_{orb}^{(M||x)}$(Fe)	$\mu_{orb}^{(M||z)}$(Pt)	$\mu_{orb}^{(M||x)}$(Pt)
	on-site	1.7		0.103	0.095	0.088	0.115
	FR-PP	2.0		0.096	0.093	0.097	0.105
Bulk FePt-L1$_0$	VASP	2.13		0.069	0.068	0.058	0.071
	FP-LMTO [53]	4.0		0.070	0.070	0.050	0.060
	SPRKKR [54]	3.04		0.065	0.062	0.044	0.042
	WIEN2K [54]	2.73		0.065	0.062	0.060	0.054
	on-site	25.1	25.8	0.081	0.075	0.137	0.173
Fe$_{24}$Pt$_{31}$ NP	FR-PP	34.0	37.2	0.072	0.068	0.132	0.170
	VASP	47.4	50.0	0.051	0.042	0.094	0.125

tion without tilt. In both SOC formalisms, the average values are $MM_{Fe} = 3.4 \mu_B/at$ and $MM_{Pt} = 0.38 \mu_B/at$. In VASP the average values of the MMs are $3.3 \mu_B/at$ and $0.5 \mu_B/at$ for Fe and Pt, respectively. The tilts along the x and y direction ranges between 0.0–$0.45 \mu_B$.

V. CONCLUSIONS

We have performed an in-depth study on the accuracy of the so-called on-site approximation for the inclusion of SOC in electronic structure calculations within the DFT-PP formalism. Within a TB spirit, this approximation assumes that all the SOC transferred to the valence electrons occurs within each ion, i.e., equivalent to the renormalization of the on-site energies together with the inclusion of intra-atomic SOC matrix elements, whereas in a more general framework SOC matrix elements between two orbitals centered at different atoms pick up contributions from neighboring atoms via three-center integrals—the full FR-PP formulation.

We have considered a variety of systems with different dimensionalities, all of them presenting strong SOC-related effects. In most cases the on-site approximation yielded good agreement with the more general full FR-PP formalism, but there were (a few) exceptions. One of them is an erroneous location of the Dirac point of the TSS at the Bi_2Se_3 (0001) surface, as it ends up below the top of the valence band and, hence, becomes n doped. Although the magnitude of this energy deviation falls within the error bars associated to DFT itself, we emphasize that it originates solely from the neglect of interatomic SOC interactions as the band structures for both approaches have been computed under the same calculation parameters.

A larger and systematic error was, however, found for $5d$ transition metals, for which the on-site band structures showed giant energy shifts—especially in the case of Ir(111)—leading to an imprecise description of the projected gaps or the offsets of surface states. By noting that most of the systems where the on-site approximation worked correctly involved states of p character around the Fermi level, we may conclude that it breaks down for systems involving $5d$-$5d$ interaction. In fact, this is not a surprising result, as these states present a large

SOC but are also spatially quite extended, so that their contribution to three-center integrals of the $\langle \mu | V_k^{so} | \nu \rangle$ type, with the AOs residing at different sites than k, is not negligible. This could also be the reason why the on-site approximation shows more sensitivity to the basis set, giving worse results when the radial extension of the basis orbitals is increased, as dramatically illustrated for the WS_2 monolayer.

We have also calculated the MAEs for a Pt dimer, a FePt-$L1_0$ cuboctahedral NP composed of 55 atoms and for FePt-$L1_0$ bulk comparing the SIESTA MAEs versus those derived with VASP for the last two systems. Although the on-site approximation predicts correctly the easy magnetization axis, the MAE values are for both systems underestimated compared with the full FR-PP formalism and VASP. MAE values for the Pt dimer are similar for both formulations.

Finally, we note that, in DFT-PP calculations, the time consumed in the construction of the SOC Hamiltonian, including all the integrals for the off-site matrix elements, represents a very small fraction of the total in a self-consistent calculation. Hence, the computational gain in using the on-site approximation is negligible and does not seem to justify its use as it is susceptible to some inaccuracies. We conclude that it is advisable to employ the full FR-PP approach with no approximations.

[1] J. Stöhr and H. C. Siegmann, *Magnetism* (Springer, Berlin, 2006).

[2] C. Cohen-Tannoudji, B. Diu, and F. Laloe, *Quantum Mechanics Vol. 1 & 2* (John Wiley & Sons Inc, New York, 1977).

[3] J. Sławińska and J. I. Cerdá, Phys. Rev. B **98**, 075436 (2018).

[4] M. Z. Hasan and C. L. Kane, Rev. Mod. Phys. **82**, 3045 (2010).

[5] C.-Z. Chang, J. Zhang, X. Feng, J. Shen, Z. Zhang, M. Guo, K. Li, Y. Ou, P. Wei, L.-L. Wang, Z.-Q. Ji, Y. Feng, S. Ji, X. Chen, J. Jia, X. Dai, Z. Fang, S.-C. Zhang, K. He, Y. Wang *et al.* Science **340**, 167 (2013).

[6] J. Sinova, S. O. Valenzuela, J. Wunderlich, C. H. Back, and T. Jungwirth, Rev. Mod. Phys. **87**, 1213 (2015).

[7] R. Cuadrado and R. W. Chantrell, Phys. Rev. B **86**, 224415 (2012).

[8] C. Antoniak, M. E. Gruner, M. Spasova, A. V. Trunova, F. Römer, A. Warland, B. Krumme, K. Fauth, S. Sun, P. Entel, M. Farle, and H. Wende, Nat. Commun. **2**, 528 (2011).

[9] R. Cuadrado, T. J. Klemmer, and R. W. Chantrell, Appl. Phys. Lett. **105**, 152406 (2014).

[10] R. Cuadrado, K. Liu, T. J. Klemmer, and R. W. Chantrell, Appl. Phys. Lett. **108**, 123102 (2016).

[11] T. Bose, R. Cuadrado, R. F. L. Evans, R. V. Chepulskii, D. Apalkov, and R. W. Chantrell, J. Phys.: Condens. Matter **28**, 156003 (2016).

[12] I. Dzyaloshinsky, J. Phys. Chem. Solids **4**, 241 (1958).

[13] T. Moriya, Phys. Rev. **120**, 91 (1960).

[14] H. Yang, A. Thiaville, S. Rohart, A. Fert, and M. Chshiev, Phys. Rev. Lett. **115**, 267210 (2015).

[15] S. Fukami, T. Anekawa, C. Zhang, and H. Ohno, Nat. Nanotechnol. **11**, 621 (2015).

[16] Y. Fan, P. Upadhyaya, X. Kou, M. Lang, S. Takei, Z. Wang, J. Tang, L. He, L.-T. Chang, M. Montazeri, G. Yu, W. Jiang, T. Nie, R. N. Schwartz, Y. Tserkovnyak, and K. L. Wang, Nat. Mater. **13**, 699 (2014).

[17] P. Gambardella and I. M. Miron, Phil. Trans. R. Soc. A **369**, 3175 (2011).

[18] http://www.flapw.de.

[19] D. R. Hamann, M. Schlüter, and C. Chiang, Phys. Rev. Lett. **43**, 1494 (1979).

[20] L. Kleinman, Phys. Rev. B **21**, 2630 (1980).

[21] J. M. Soler, E. Artacho, J. D. Gale, A. García, J. Junquera, P. Ordejón, and D. Sánchez-Portal, J. Phys.: Condens. Matter **14**, 2745 (2002).

[22] G. Kresse and J. Furthmüller, J. Comput. Mater. Sci. **6**, 15 (1996).

[23] P. Giannozzi, S. Baroni, N. Bonini, M. Calandra, R. Car, C. Cavazzoni, D. Ceresoli, G. L. Chiarotti, M. Cococcioni, I. Dabo, A. D. Corso, S. de Gironcoli, S. Fabris, G. Fratesi, R. Gebauer, U. Gerstmann, C. Gougoussis, A. Kokalj, M. Lazzeri, L. Martin-Samos *et al.*, J. Phys.: Condens. Matter **21**, 395502 (2009).

[24] P. Giannozzi, O. Andreussi, T. Brumme, O. Bunau, M. B. Nardelliuongiorno, M. Calandra, R. Car, C. Cavazzoni, D. Ceresoli, M. Cococcioni, N. Colonna, I. Carnimeo, A. Dal Corso, S. de Gironcoli, P. Delugas, R. A. DiStasio, A. Ferretti, A. Floris, G. Fratesi, G. Fugallo, R. Gebauer, U. Gerstmann *et al.*. J. Phys.: Condens. Matter **29**, 465901 (2017).

[25] L. A. Hemstreet, C. Y. Fong, and J. S. Nelson, Phys. Rev. B **47**, 4238 (1993).

[26] R. Cuadrado and J. I. Cerdá, J. Phys.: Condens. Matter **24**, 086005 (2012).

[27] L. Kleinman and D. M. Bylander, Phys. Rev. Lett. **48**, 1425 (1982).

[28] H. Aramberri, J. I. Cerdá, and M. C. Muñoz, Nanoletters **15**, 3840 (2015).

[29] R. Cuadrado, M. Pruneda, A. García, and P. Ordejón, J. Phys.: Mater. **1**, 015010 (2018).

[30] L. Fernández–Seivane and J. Ferrer, Phys. Rev. Lett. **99**, 183401 (2007).

[31] L. Fernández–Seivane, M. A. Oliveira, S. Sanvito, and J. Ferrer, J. Phys: Condens. Matter **18**, 7999 (2009).

[32] K. Kurita and T. Koretsune, Phys. Rev. B **102**, 045109 (2020)

[33] S. Konschuh, M. Gmitra, and J. Fabian, Phys. Rev. B **82**, 245412 (2010).

[34] K. Song, D. Soriano, A. W. Cummings, D. Robles, P. Ordejón, and S. Roche, Nanoletters **18**, 2033 (2018).

[35] A. García, N. Papior, A. Akhtar, E. Artacho, V. Blum, E. Bosoni, P. Brandimarte, M. Brandbyge, J. I. Cerdá, F. Corsetti, R. Cuadrado, V. Dikan, J. Ferrer, J. Gale, P. García-Fernández, V. M. García-Suárez, S. García, G. Huhs, S. Illera, R. Korytár *et al.*, J. Chem. Phys. **152**, 204108 (2020).

[36] S. G. Louie, S. Froyen, and M. L. Cohen, Phys. Rev. B **26**, 1738 (1982).

[37] M. J. van Setten, M. Giantomassi, E. Bousquet, M. J. Verstraete, D. R. Hamann, X. Gonze, and G. M. Rignanese, Comput. Phys. Commun. **226**, 39 (2018).

[38] See http://www.pseudo-dojo.org.

[39] J. P. Perdew, K. Burke, and M. Ernzerhof, Phys. Rev. Lett. **77**, 3865 (1996).

[40] E. Artacho, D. Sánchez-Portal, P. Ordejón, A. García, and J. M. Soler, Phys. Stat. Sol. (b) **215**, 809 (1999).

[41] S. Steiner, S. Khmelevskyi, M. Marsmann, and G. Kresse, Phys. Rev. B **93**, 224425 (2016).

[42] J. Cerdá, M. A. Van Hove, P. Sautet, and M. Salmeron, Phys. Rev. B **56**, 15885 (1997).

[43] E. T. R. Rossen, C. F. J. Flipse, and J. I. Cerdá, Phys. Rev. B **87**, 235412 (2013).

[44] J. Han, A. Zhang, M. Chen, W. Gao, and Q. Jiang, Nanoscale **12**, 10277 (2020).

[45] X. Li, H. Liu, H. Jiang, F. Wang, and J. Feng, Phys. Rev. B **90**, 165412 (2014).

[46] S. García-Gil, A. García, N. Lorente, and P. Ordejón, Phys. Rev. B **79**, 075441 (2009).

[47] R. Roldán, M. P. López-Sancho, F. Guinea, E. Cappelluti, J. A. Silva-Guillén, and P. Ordejón, 2D Mater. **1**, 034003 (2014).

[48] S. LaShell, B. A. McDougall, and E. Jensen, Phys. Rev. Lett. **77**, 3419 (1996).

[49] G. Nicolay, F. Reinert, S. Hüfner, and P. Blaha, Phys. Rev. B **65**, 033407 (2001).

[50] A. Mugarza, A. Mascaraque, V. Repain, S. Rousset, K. N. Altmann, F. J. Himpsel, Yu. M. Koroteev and E. V. Chulkov, F. J. García de Abajo and J. E. Ortega, Phys. Rev. B **66**, 245419 (2002).

[51] G. Dresselhaus, Phys. Rev. **100**, 580 (1955).

[52] D. Di Sante, P. Barone, R. Bertacco, and S. Picozzi, Adv. Mater. **25**, 509 (2013).

[53] I. Galanakis, M. Alouani, and H. Dreysse, Phys. Rev. B **62**, 6475 (2000).

[54] S. A. Khan, P. Blaha, H. Ebert, J. Miná, and O. Šipr, Phys. Rev. B **94**, 144436 (2016).